Astrophysics of gravitational wave sources

Lecture 13: GW170817 & “future” sources of GW

Ondřej Pejcha

ÚTF MFF UK

Binary neutron star merger

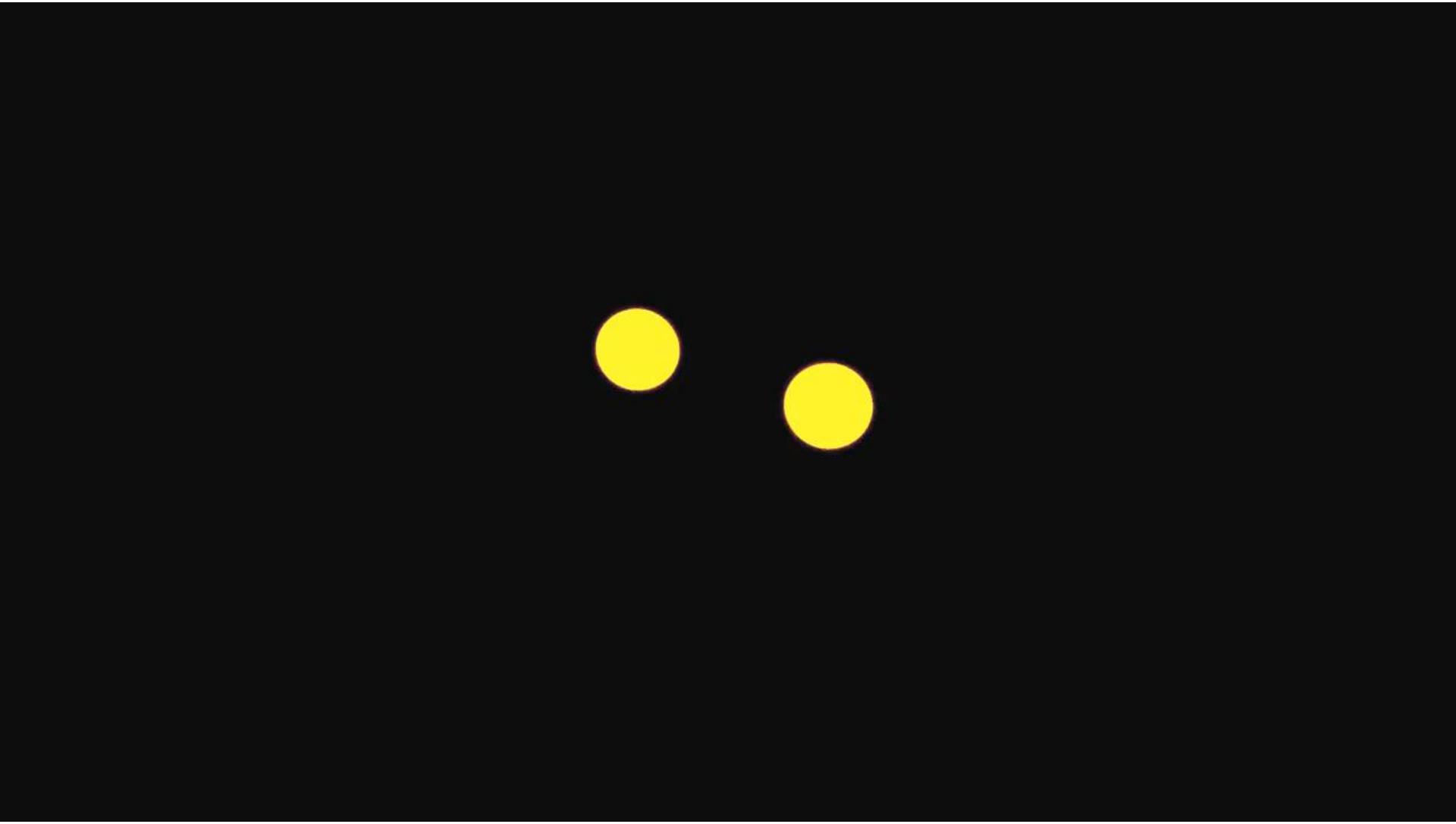

Radice et al.

Neutron star mergers

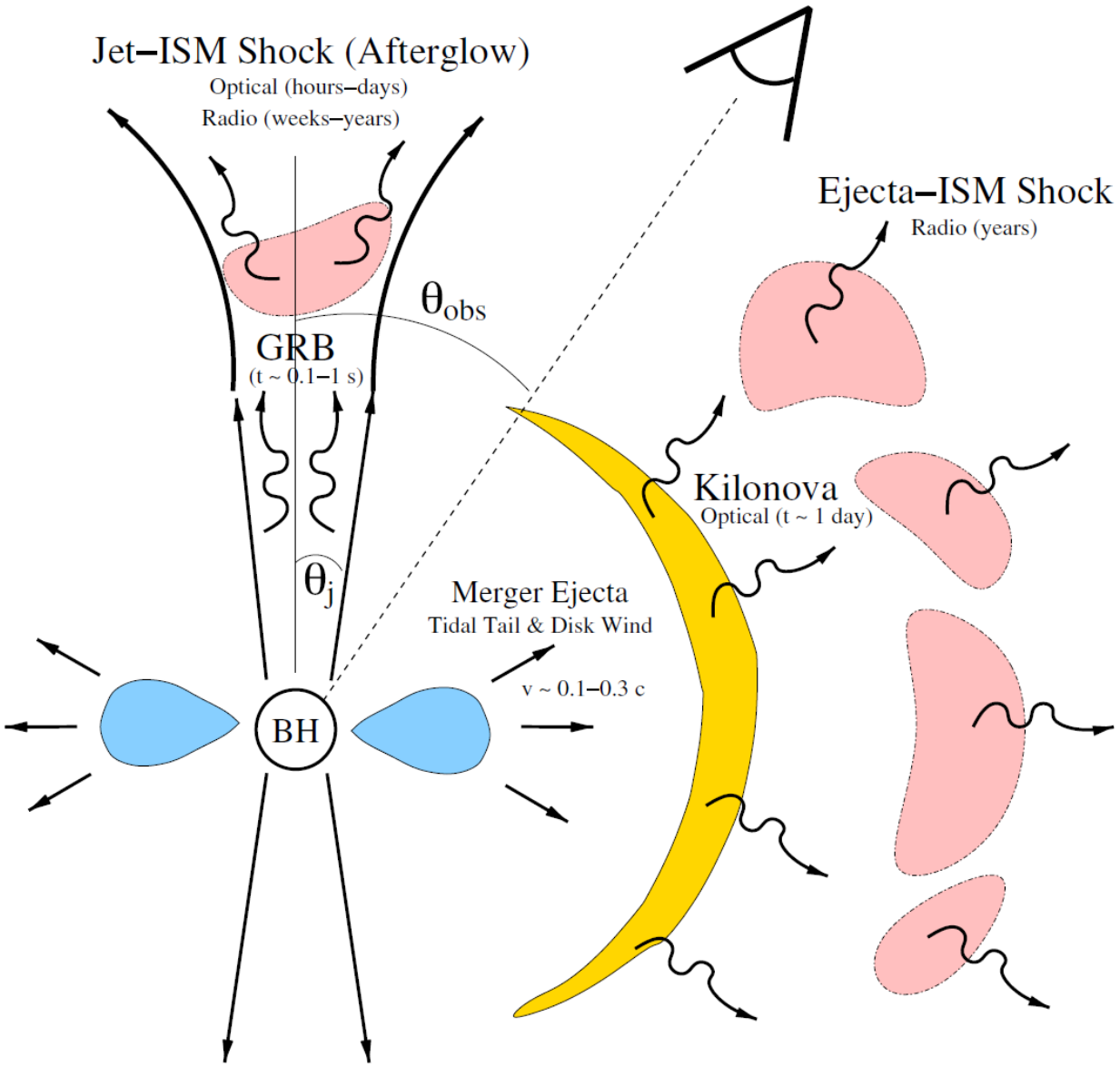

Metzger & Berger (2012)

GW170817

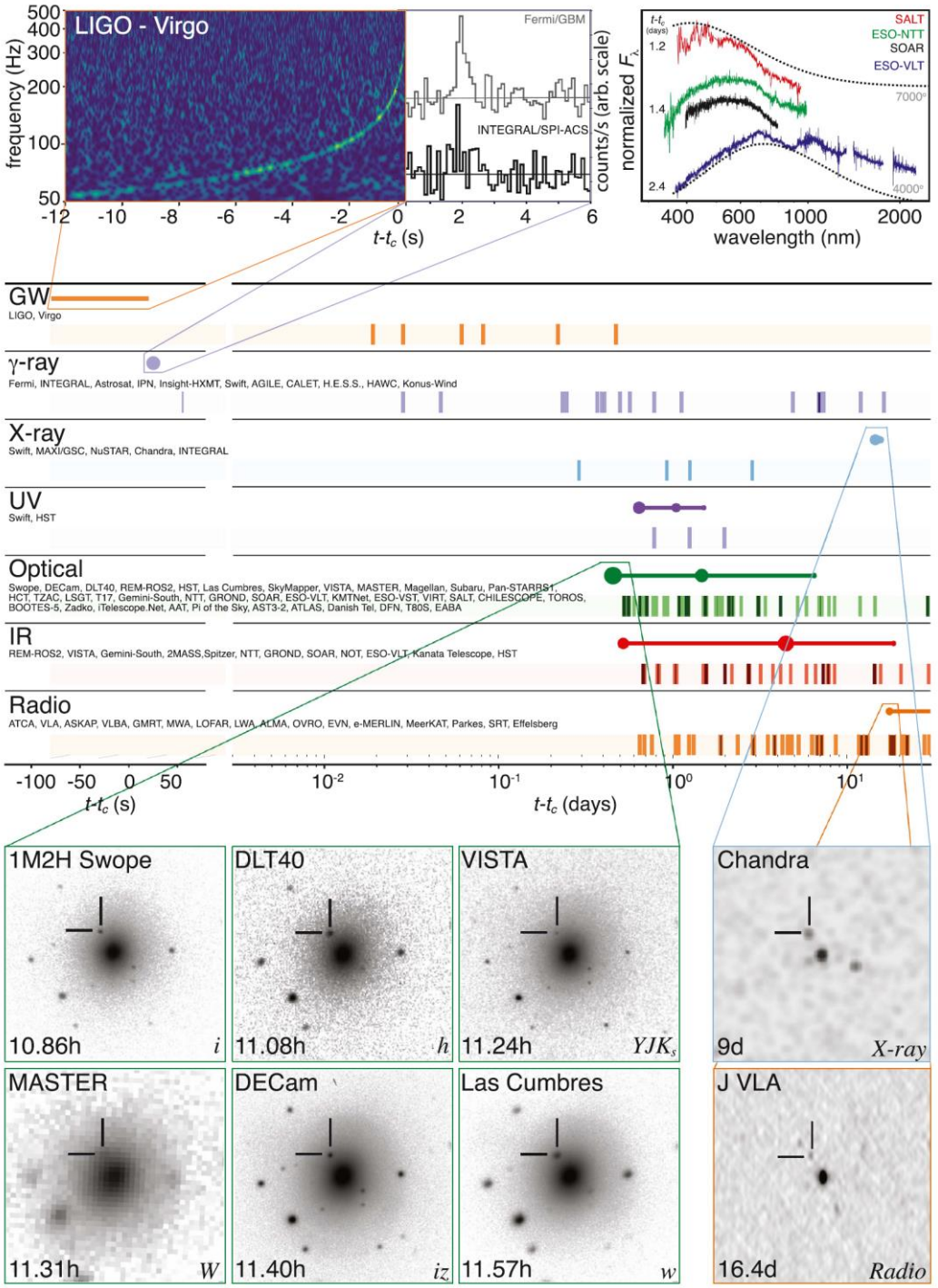

Abott et al. (2017)

Observations of GW170817

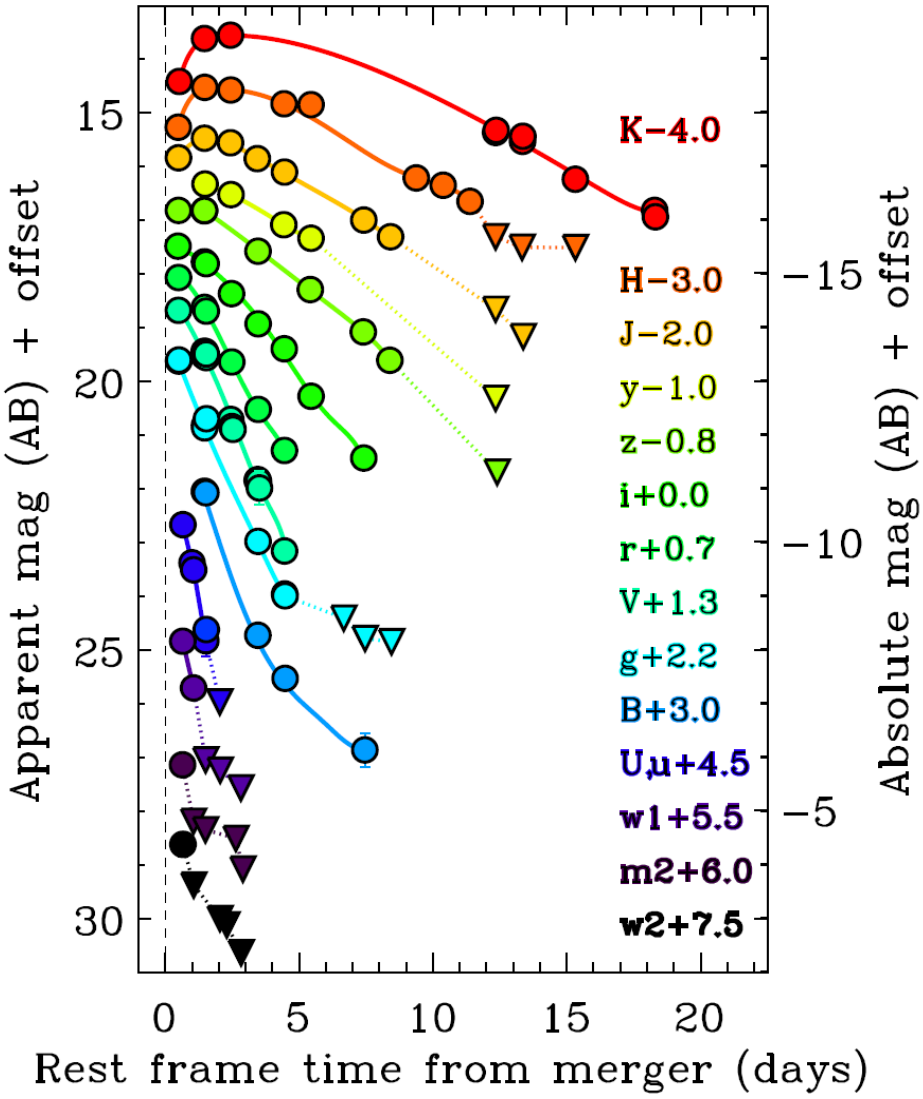

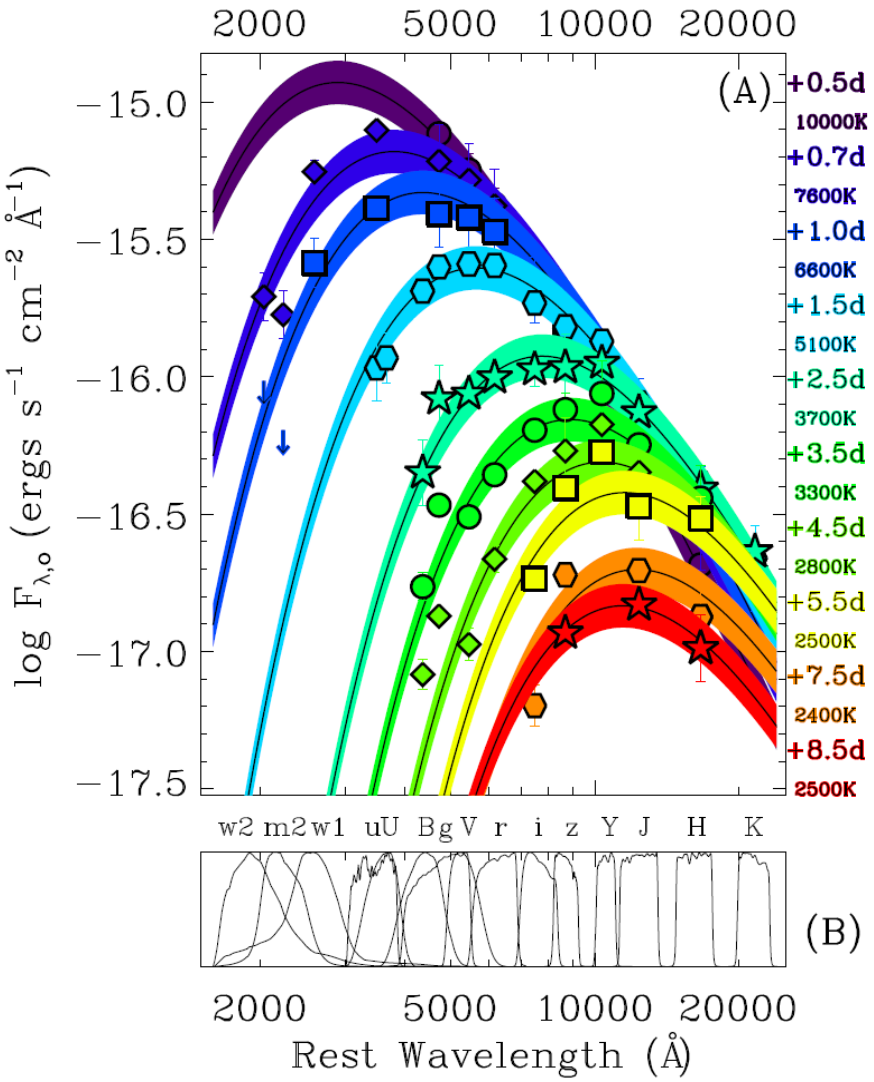

Drout et al. (2017)

$$t_{\rm lc} \approx \left(\frac{3\kappa M}{4\pi c v}\right)^{\frac{1}{2}} \approx 2.7\,{\rm days} \times \left(\frac{M}{0.01M}\right)^{\frac{1}{2}} \left(\frac{v}{0.1c}\right)^{-\frac{1}{2}} \left(\frac{\kappa}{1{\rm cm}^2\,{\rm g}^{-1}}\right)^{\frac{1}{2}} \quad (2)$$

The characteristic luminosity of the kilonova is approximately equal to the radioactive heating rate at this escape timescale

$$L_{\rm lc} \approx M\varepsilon_{\rm nuc}(t_{\rm lc}) \approx 5\times10^{40}\,{\rm erg\,s^{-1}} \times \left(\frac{M}{0.01M}\right)^{1-\frac{\alpha}{2}} \left(\frac{v}{0.1c}\right)^{\frac{\alpha}{2}} \left(\frac{\kappa}{1{\rm cm}^2\,{\rm g}^{-1}}\right)^{-\frac{\alpha}{2}} \quad (3)$$

A larger ejecta mass produces a brighter and longer-lasting kilonova; a higher velocity gives a brighter and briefer kilonova.

Observable signatures of heavy element formation

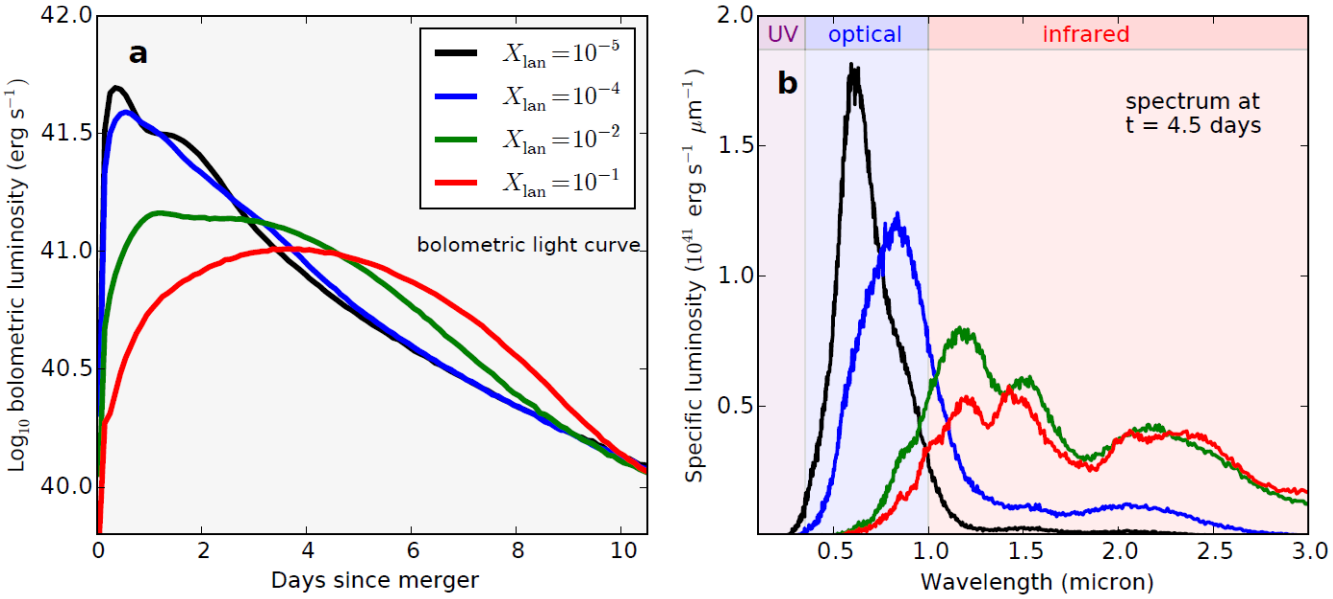

Figure 2 | Models of kilonovae demonstrating the observable signatures of r-process abundances. All models have an ejecta mass $M = 0.05M_{\odot}$ and velocity $v_{\rm k} = 0.2c$, but different mass fractions of lanthanides $X_{\rm lan}$. **a**, Model bolometric light curves. If the ejecta is composed primarily of heavier r-process material ($X_{\rm lan} \geq 10^{-2}$) the opacity is higher, resulting in a longer diffusion times and longer duration bolometric light curves. **b**, Model spectra as observed 4.5 d after the mergers. The higher lanthanide opacities of the heavy r-process materials obscure the optical bands and shift the emission primarily to the infrared.

Kasen et al. 2017

What can we learn from a spectrum of kilonova?

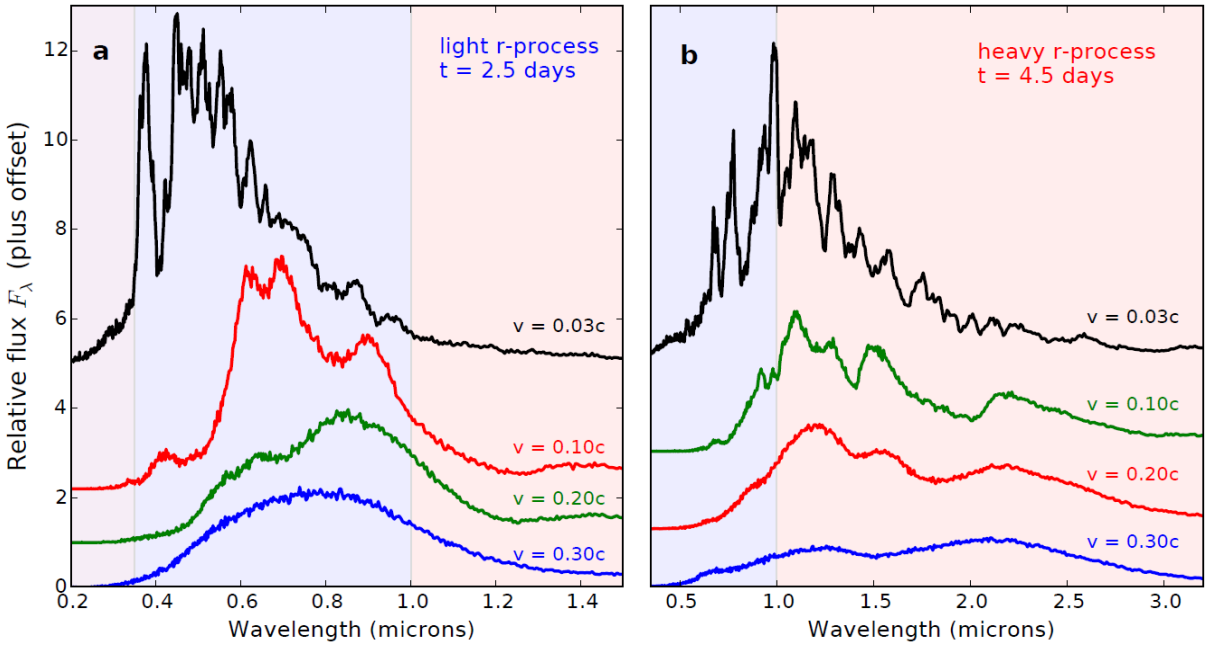

Figure 3 | Models of kilonovae demonstrating the spectral diagnostics of the ejecta velocity. The models all have ejecta mass $M = 0.03M_\odot$. **a**, Spectra of models composed of light r-process material ($X_{\rm lan} = 10^{-4}$) observed 1.5 d after the merger. Modest ejecta velocities ($v_{\rm k} = 0.03c$, typical of supernovae) produce conspicuous absorption spectral features. At higher velocities ($v_{\rm k} = 0.1c$–$0.2c$) the features are broadened and blended, while for $v_{\rm k} = 0.3c$ the spectra are essentially featureless. The optical spectra of AT 2017gfo were featureless, implying a high-velocity, approximately $0.3c$ component of light r-process ejecta. **b**, Spectra of models composed of heavy r-process material ($X_{\rm lan} = 10^{-2}$) observed 3.5 d after the merger. The infrared spectra of AT 2017gfo showed broad peaks, implying a lower-velocity, approximately $0.1c$ component of heavy r-process ejecta.

Kasen et al. (2017)

What can we learn from a spectrum of kilonova?

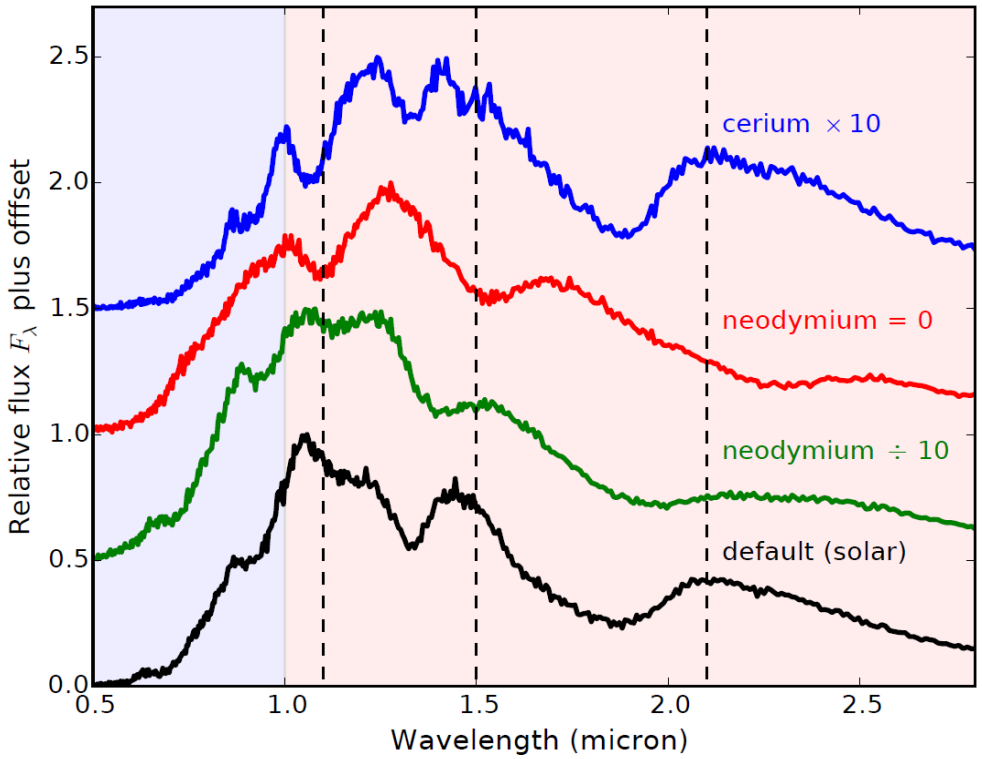

Figure 4 | Models demonstrating how kilonova spectral features probe the abundance of individual r-process elements. The spectral peaks in the models are blends of many lines, primarily those of the complex lanthanide species. The default model shown (parameters $M = 0.04M_\odot$, $v_k = 0.15c$, $X_{lan} = 10^{-1.5}$) uses a solar distribution of lanthanides, and has spectral peaks near 1.1 μm, 1.5 μm and 2.0 μm (marked with dashed lines). These features are mainly attributable to neodymium ($Z = 60$) given that reducing or removing this species changes the feature locations. However, other lanthanides such as cerium ($Z = 58$) also affect the blended peaks. Uncertainties in the current atomic line data sources limit hinder spectral analysis, but with improved atomic inputs a more detailed compositional breakdown is within reach.

Kasen et al. (2017)

Observations of GW170817

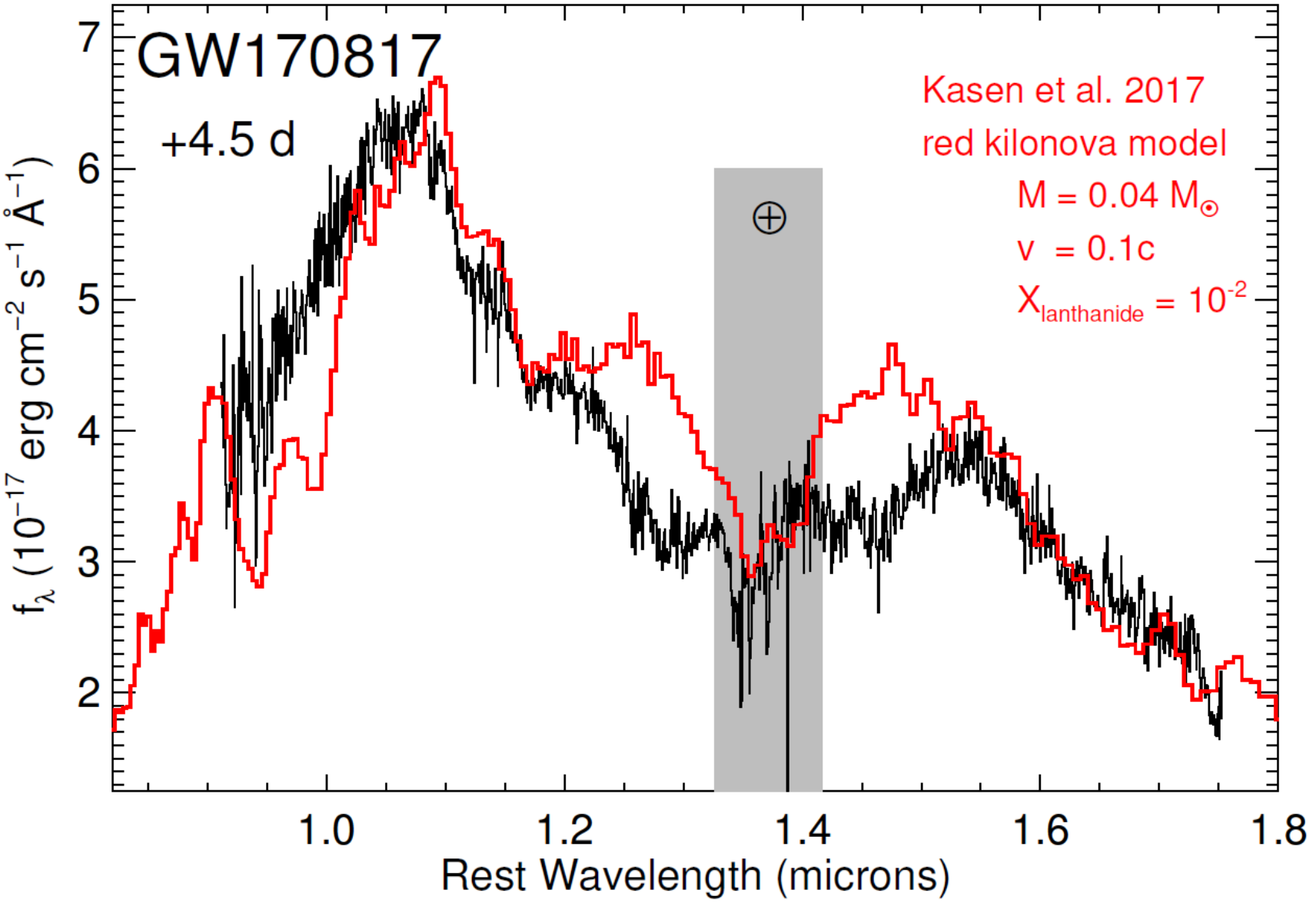

Chornock et al. 2017

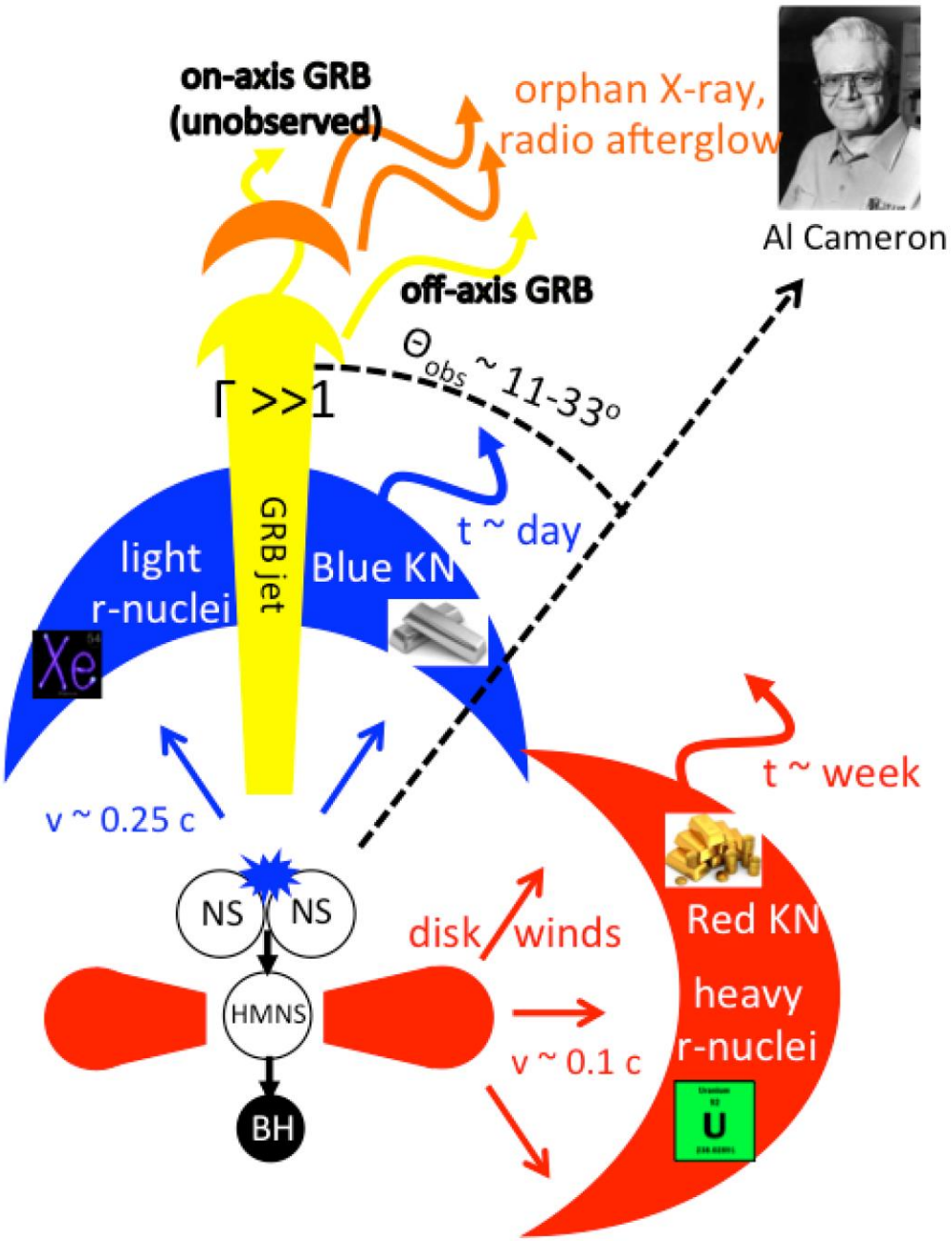

Metzger 2017

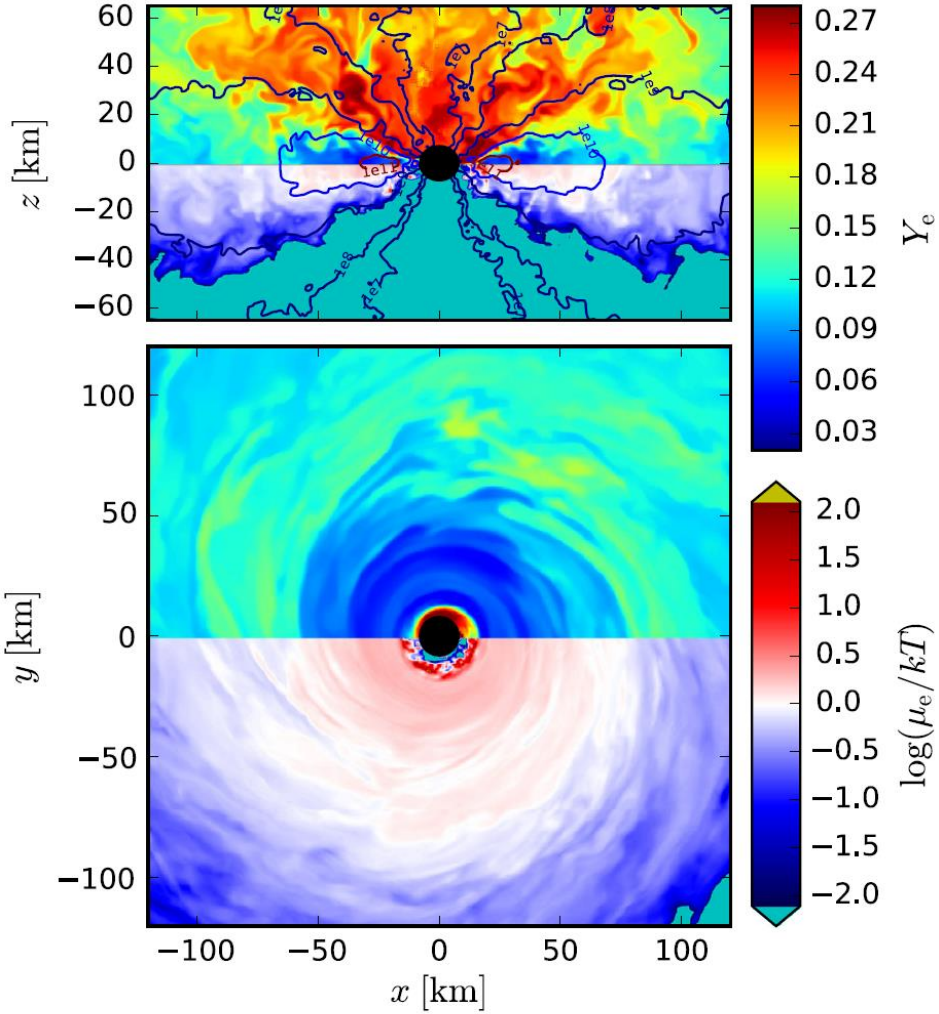

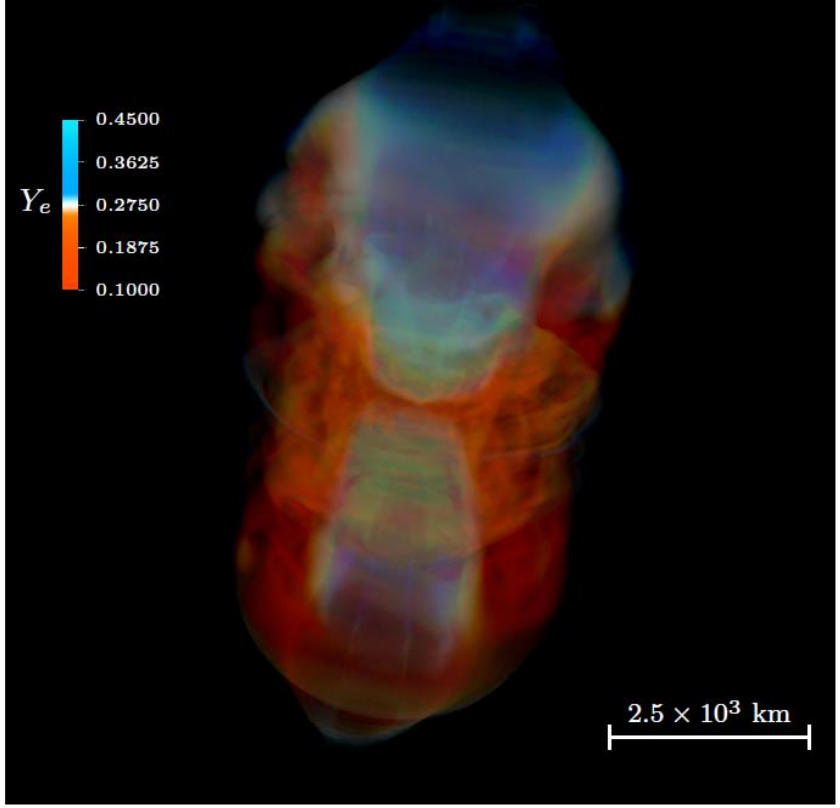

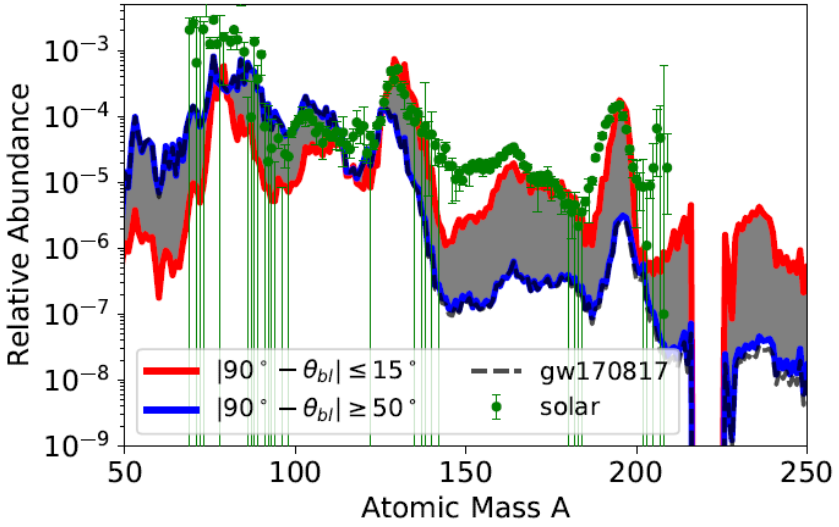

Over the 380-ms duration of the simulation, we find that a fraction ≈20% of the initial torus mass is unbound in powerful outflows with asymptotic velocities v ≈ 0.1c and electron fractions $Y_e \approx 0.1–0.25$.

Siegel & Metzger (2017)

Miller et al. (2019)

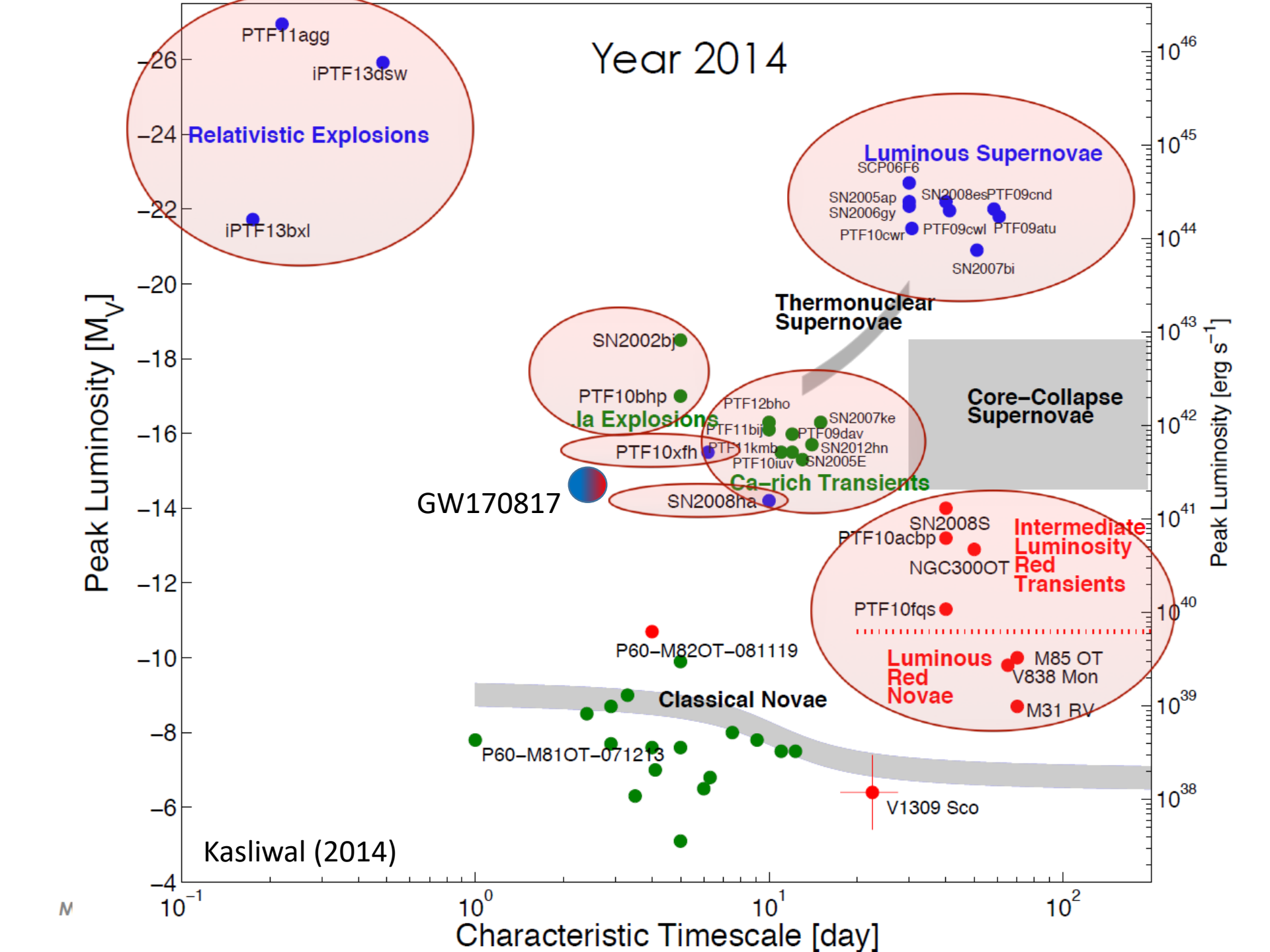
Year 2014
PTF11agg
iPTF13dsw
Relativistic Explosions
iPTF13bxl
Luminous Supernovae
SCP06F6
SN2005ap
SN2006gy
SN2008es
PTF09cnd
PTF10cwr
PTF09cwl
PTF09atu
SN2007bi
Thermonuclear Supernovae
SN2002bj
PTF10bhp
Ia Explosions
PTF10xfh
PTF12bho
PTF11bij
PTF11kmb
PTF10iuv
SN2007ke
PTF09dav
SN2012hn
SN2005E
Ca-rich Transients
SN2008ha
Core-Collapse Supernovae
GW170817
SN2008S
PTF10acbp
NGC300OT
Intermediate Luminosity Red Transients
PTF10fqs
P60-M82OT-081119
Luminous Red Novae
M85 OT
V838 Mon
M31 RV
Classical Novae
P60-M81OT-071213
V1309 Sco
Kasliwal (2014)
Peak Luminosity [M_V]
Peak Luminosity [erg s^-1]
Characteristic Timescale [day]

Gravitational Wave Detectors and Sources

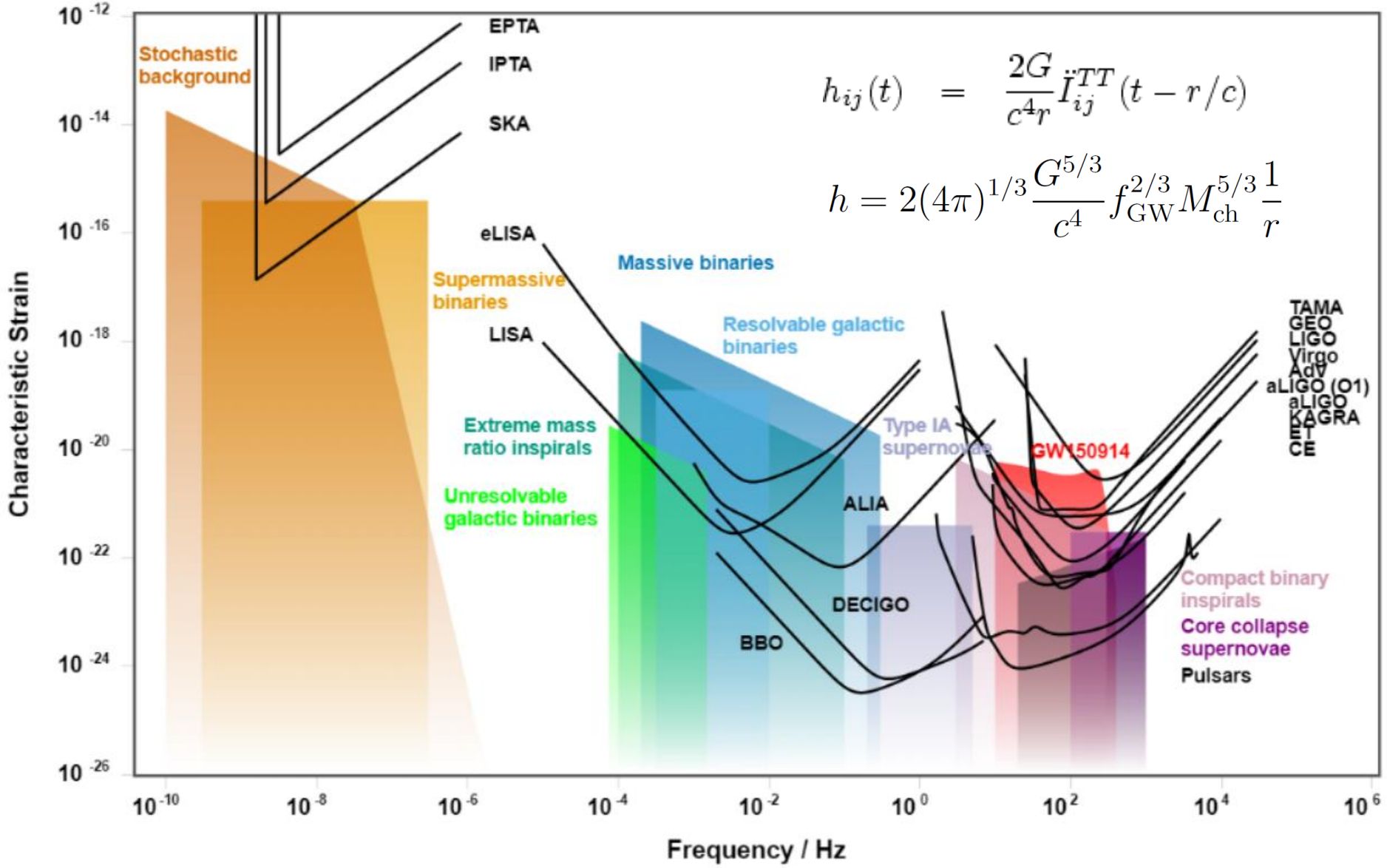

$$h_{ij}(t) = \frac{2G}{c^4 r}\ddot{I}_{ij}^{TT}(t - r/c)$$

$$h = 2(4\pi)^{1/3}\frac{G^{5/3}}{c^4}f_{\mathrm{GW}}^{2/3}M_{\mathrm{ch}}^{5/3}\frac{1}{r}$$

gwplotter.com

Binary objects

- Binary neutron stars / black holes
- White dwarfs
- EMRIs = Extreme Mass-ratio Inspirals
- Supermassive black holes

Core-collapse supernovae

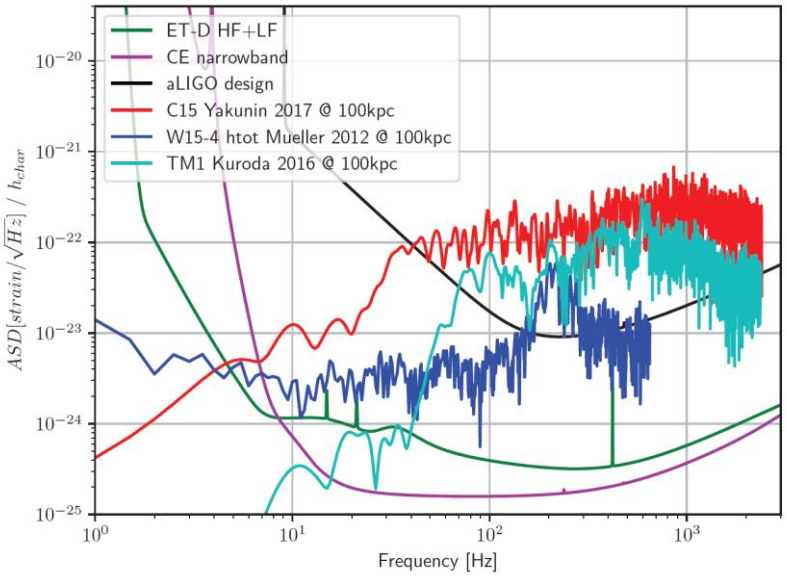

Kalogera et al. (2019)

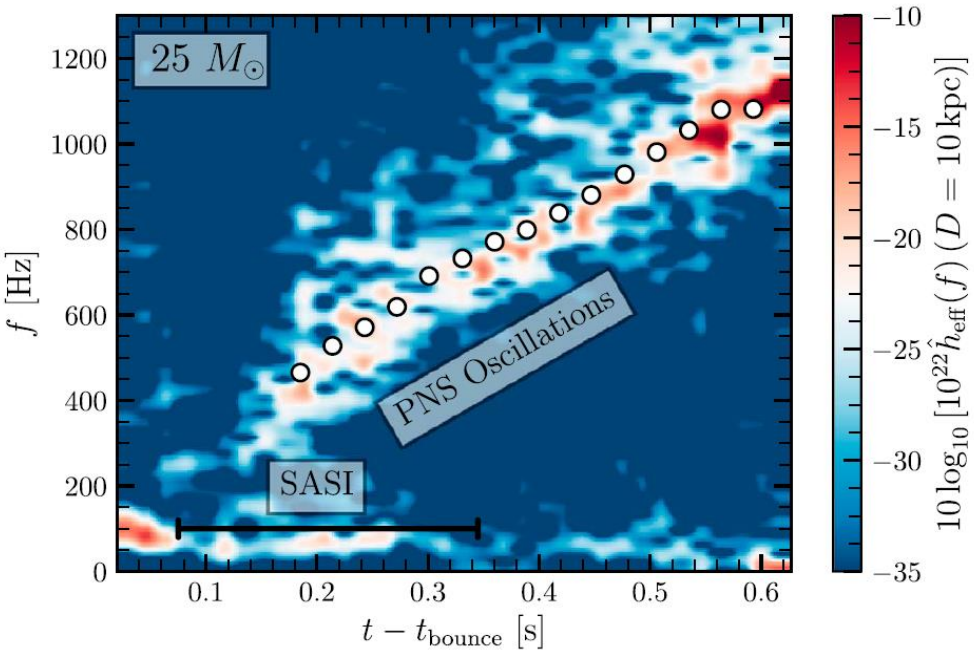

Figure 5. Time–frequency content of the GW signal for the 25 $M_\odot$ progenitor. The white dots denote the eigenfrequencies associated with the quadrupolar f- and low-order, $n = 1$, 2, g-modes of the PNS as computed from linear perturbation theory. This progenitor is the only one in our set showing a clear signature of the SASI at low frequency. The presence of a higher-frequency component associated with PNS oscillations is instead universal.

Radice et al. (2019)

GW also from accreting NS and other surface processes on NS

Stochastic GW background

Unresolved sources of cosmological and astrophysical origin, redshifted accordingly to their emission epoch

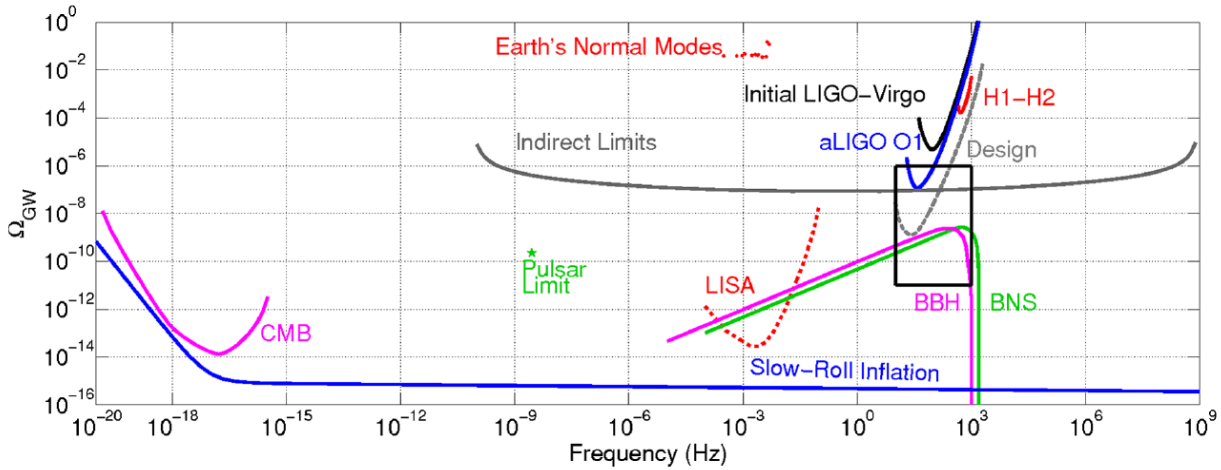

FIG. 3. Presented, here, are constraints on the background in PI form [59], as well as some representative models, across many decades in frequency. We compare the limits from ground-based interferometers from the final science run of Initial LIGO-Virgo, the colocated detectors at Hanford (H1–H2), Advanced LIGO (aLIGO) O1, and the projected design sensitivity of the advanced detector network assuming two years of coincident data, with constraints from other measurements: CMB measurements at low multipole moments [60], indirect limits from the cosmic microwave background (CMB) and big bang nucleosynthesis [61,62], pulsar timing [62], and from the ringing of Earth's normal modes [63]. We also show projected limits from a space-based detector such as LISA [59,64,65], following the assumptions of [59]. We extend the BNS and BBH distributions using an $f^{2/3}$ power-law down to low frequencies, with a low-frequency cutoff imposed where the inspiral time scale is of the order of the Hubble scale. In Fig. 5, we show the region in the black box in more detail.

Abott et al. (2017)

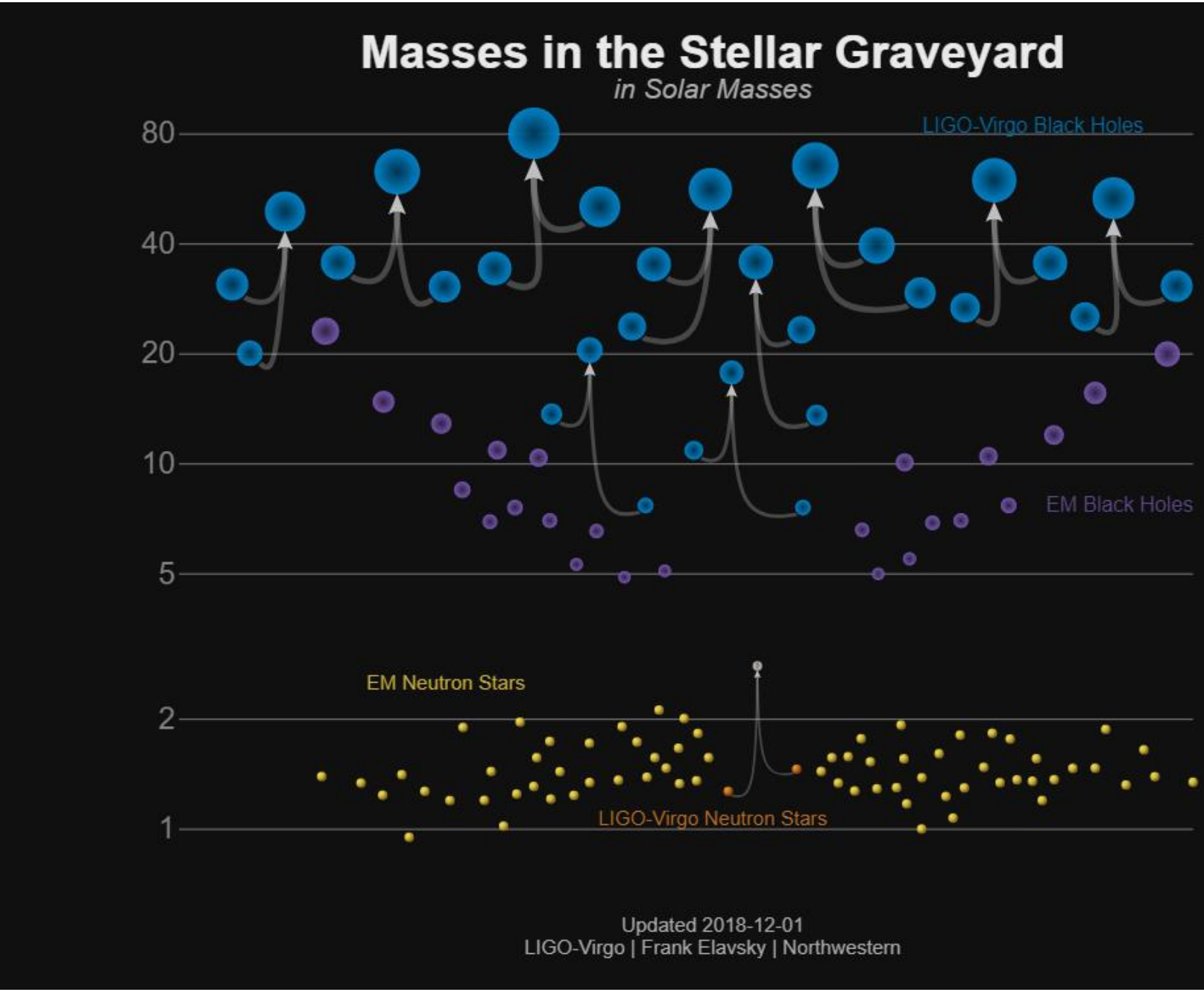
Masses in the Stellar Graveyard
in Solar Masses
80
40
20
10
5
2
1
LIGO-Virgo Black Holes
EM Black Holes
EM Neutron Stars
LIGO-Virgo Neutron Stars
Updated 2018-12-01
LIGO-Virgo | Frank Elavsky | Northwestern

The Origin of the Solar System Elements

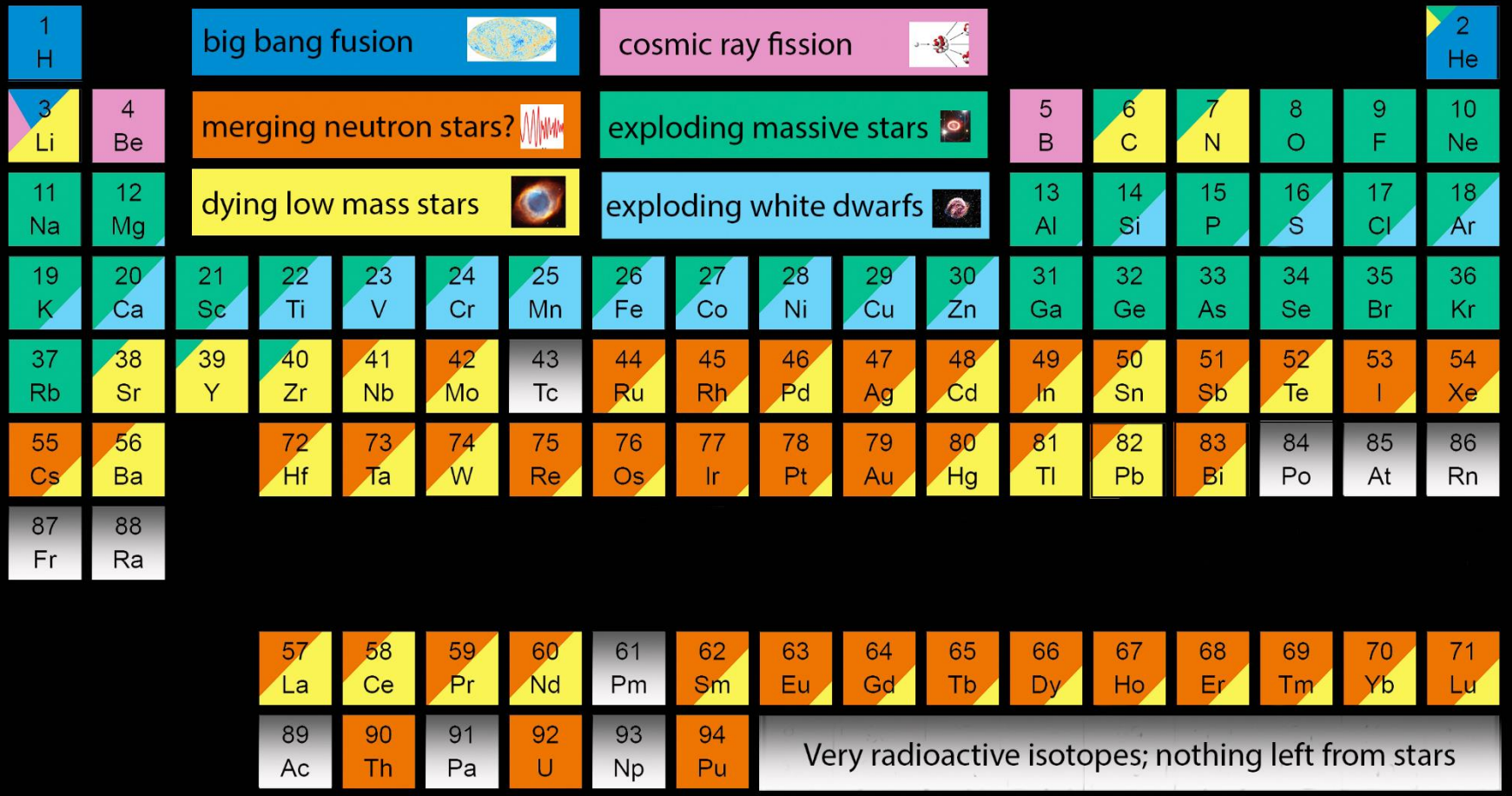

Graphic created by Jennifer Johnson
http://www.astronomy.ohio-state.edu/~jaj/nucleo/

Astronomical Image Credits:
ESA/NASA/AASNova